PHYSICAL REVIEW APPLIED **15,** 044051 (2021)

Correlation Between Corrugation-Induced Flexoelectric Polarization and Conductivity of Low-Dimensional Transition Metal Dichalcogenides

Anna N. Morozovska,[1,*] Eugene A. Eliseev,[2] Hanna V. Shevliakova,[1,3] Yaroslava Yu. Lopatina,[1]
Galina I. Dovbeshko,[1] Maya D. Glinchuk,[2] Yunseok Kim,[4,†] and Sergei V. Kalinin[5,‡]

[1] *Institute of Physics, National Academy of Sciences of Ukraine, 46, pr. Nauky, 03028 Kyiv, Ukraine*
[2] *Institute for Problems of Materials Science, National Academy of Sciences of Ukraine, Krjijanovskogo 3, 03142 Kyiv, Ukraine*
[3] *Department of Microelectronics, National Technical University of Ukraine "Igor Sikorsky Kyiv Polytechnic Institute", Kyiv, Ukraine*
[4] *School of Advanced Materials Science and Engineering, Sungkyunkwan University (SKKU), Suwon 16419, Republic of Korea*
[5] *The Center for Nanophase Materials Sciences, Oak Ridge National Laboratory, Oak Ridge, Tennessee 37922, USA*

(Received 7 December 2020; revised 11 February 2021; accepted 29 March 2021; published 29 April 2021)

The tunability of polar and semiconducting properties of low-dimensional transition metal dichalcogenides (TMDs) have propelled them to the forefront of fundamental and applied physical research. These materials can vary their electrophysical properties from nonpolar to ferroelectric, and from direct-band semiconducting to metallic. In addition to classical controlling factors, such as field effect, composition, and doping, new degrees of freedom emerge in TMDs due to the curvature-induced electron redistribution and the associated changes in electronic properties.

Here we theoretically explore the elastic and electric fields, flexoelectric polarization and free charge density for a TMD nanoflake placed on a rough substrate with a sinusoidal corrugation profile. Finite element modelling results for different flake thickness and corrugation depth yield insights into the flexoelectric nature of the out-of-plane electric polarization and establish the unambiguous correlation between the polarization and static conductivity modulation. The modulation is caused by the coupling between the deformation potential and inhomogeneous elastic strains, which evolve in the TMD nanoflake due to the adhesion between the flake surface and corrugated substrate.

We reveal a pronounced maximum in the thickness dependences of the electron and hole conductivity of MoS_2 and $MoTe_2$ nanoflakes placed on a corrugated substrate, which opens the way for the optimization of their geometry towards significant improvement in their polar and electronic properties, necessary for advanced applications in nanoelectronics and memory devices. Specifically, the obtained results can be useful for the development of nanoscale straintronic devices based on the bended MoS_2, $MoTe_2$, and MoSTe nanoflakes, such as diodes and bipolar transistors with a bending-controllable sharpness of *p*-*n* junctions.

DOI: 10.1103/PhysRevApplied.15.044051

I. INTRODUCTION

The tunability of polar and semiconducting properties of low-dimensional (LD) transition metal dichalcogenides (TMDs) with a chemical formula MX_2 (M is a metal Mo, W, Re; X is a chalcogen S, Se, Te) [1,2] and Janus compounds (JCs) with a chemical formula MXY (X, Y are chalcogens) [3–5] in the form of monolayers and nanoflakes have propelled them to the forefront of fundamental and applied physical research. These materials offer a broad gamut of properties varying from nonpolar to ferroelectric, and from direct-band semiconductor to metallic. It is notable that LD semiconductor materials, such as graphene, MX_2, and MXY, are ideal candidates for strain engineering [6] and straintronics [7], because their strain-induced conductive domain walls can act as mobile charged channels, similar to the "domain wall nanoelectronics" in multiferroic thin films [8–10] and graphene-on-ferroelectric nanostructures [11,12].

Layered TMDs in the form of bulk materials are typically nonpolar centrosymmetric semiconductors with

---

[*] anna.n.morozovska@gmail.com
[†] yunseokkim@skku.edu
[‡] sergei2@ornl.gov

a relatively wide band gap of approximately 1.1–2 eV [1]. However, on transition from the bulk to the nanoscale additional orderings emerge. These orderings can be nonpolar or piezoelectric, or even ferroelectric [13–15], semiconductive, semimetallic, or metallic [16–18], as are found in different structural phases (polymorphs) of TMD monolayers. Similarly, in addition to classical controlling factors, such as field effect, composition, and doping [19], new degrees of freedom emerge in TMDs due to the curvature-induced electron redistribution and associated changes in electronic properties (see, e.g., [20,21]). In particular, there are prospective theoretical and experimental possibilities for tuning the structural, polar, and electronic properties of LD TMDs by application of homogeneous [22,23] and inhomogeneous [24,25] elastic strains. However, these possibilities are barely systematized and mostly empirical.

From the theoretical perspective, a number of first-principles studies have explored the surface-induced piezoelectricity [26,27] and ferroelectric polarization [15,28] in various MX_2. As predicted by several authors [21,29], and later discovered experimentally [24], an elastic bending can induce polar phenomena in LD TMDs, either intrinsic or induced by the external structural and charge disorder. Large curvatures enabled by small bending stiffnesses can give rise to a significant polarization induced by a flexoelectric effect [30,31]. The bending-induced out-of-plane dipole moment with density $p \sim 0.01 - 0.4$C/nm and flexoelectric polarization $P \sim 0.1 - 2\mu$C/cm^2 [32] have been calculated from first principles for MoS$_2$ [15], WS$_2$ [31], and WTe$_2$ [33,34] single layers, respectively. Therefore, it is quite possible that the strongly inhomogeneous spontaneous deformation of LD TMDs, which causes the appearance of their spontaneous polarization, is due to the flexoelectric coupling [1,24,35]. Let us focus on several recent examples.

Previously, we described analytically the structural phases of MX_2 and discussed the mechanisms of its ferroelectric state appearance using a Landau-Ginzburg-Devonshire-type (LGD-type) approach [36]. The LGD-type thermodynamic analysis suggests that out-of-plane ferroelectricity can exist in many phases of LD TMDs with a switchable polarization being proportional to the out-of-plane order parameter, and further predicts that the domain walls in LD TDMs should become conductive above a certain strain threshold. Despite the progress, the nature of one-dimensional piezoelectricity and ferroelectricity has not been elucidated, and the mesoscopic analytical theory of polar and electronic phenomena in LD TMDs has not been constructed. Such a theory is necessary to control and predict the physical properties of LD TMDs and JCs for their novel applications in nanoelectronics and advanced memory.

From a crystallographic and symmetry point of view, only the in-plane piezoelectricity can exist in a geometrically flat centrosymmetric MX_2 layer. In spite of the symmetry, tunable out-of-plane piezoelectricity induced by the local flexoelectricity was observed by Kang *et al.* [24] in semiconducting $2H$-MoTe$_2$ flakes by creating surface corrugation. The flexoelectricity induced by the surface corrugation can appear in other two-dimensional or thin-layered materials and, furthermore, the results could provide useful information on the interweaving relationship between mechanical stimulus and electric dipole in LD materials. Next, Kang *et al.* [1] demonstrated the creation of strong out-of-plane piezoelectricity in semiconducting $2H$-MoTe$_2$ flakes by artificial atomic-scale symmetry breaking realized through Te vacancy formation, and confirmed by density functional theory (DFT) calculations.

Recently [35] we developed a LGD-type theory for the description of polar phenomena in LD TMDs, specifically exploring the flexoelectric origin of the polarization induced by a spontaneous bending and by inversion symmetry breaking due to interactions with the substrate. We consider the appearance of the spontaneous out-of-plane polarization due to the flexoelectric coupling with the strain gradient of the spontaneous surface rippling and surface-induced piezoelectricity in TMD single layers. The performed calculations proved that the out-of-plane spontaneous polarization, which originated from the flexoelectric effect in a rippled TMD, is bistable and can be reversed by a nonuniform electric field.

This work is devoted to the establishment of a correlation between polar and electronic properties of LD TMDs and JCs, which is almost unexplored. Using finite element modeling (FEM) we calculate the elastic and electric fields, flexoelectric polarization, and free charge density for a TMD (or JC) nanoflake placed on a rough substrate with a sinusoidal corrugation profile. Analysis of FEM results obtained for different flake thicknesses (varying from 10 to 300 nm in accordance with experiment [24]) and corrugation depth (varying from 0 to 50 nm according to typical technological conditions [37]), allows corroboration of the flexoelectric nature of the out-of-plane electric polarization and establishes the unambiguous correlation between the polarization and static conductivity modulation.

II. THEORETICAL MODEL AND MATERIAL PARAMETERS

Here we explore the effect of bending-induced flexoelectric polarization of MX_2 nanoflakes originating from the adhesion to a corrugated substrate. For JCs, the flexoelectric polarization can be superposed with the piezoelectric polarization coming from inversion symmetry breaking at the MXY surface. The overall picture of the bending-induced flexoelectric polarization and surface-induced piezoelectric polarization in and MX_2 and MXY is shown schematically in Fig. 1.

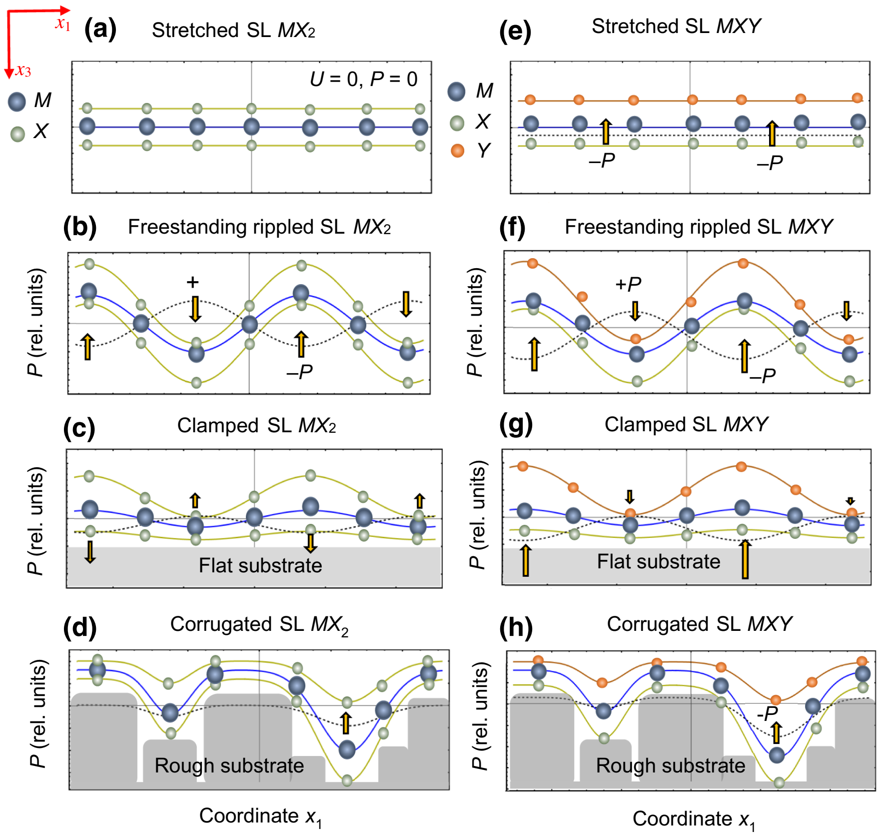

FIG. 1. Bending-induced out-of-plane polarization in a SL MX_2 (a)–(d) and JC MXY (e)–(h). M is a transition metal, X and Y are chalcogen atoms. M ions are positively charged, X and Y ions are negatively charged. Orange arrows indicate the direction of emerging out-of-plane dipole polarization P, with a profile shown by a dashed black curve. A relative atomic displacement U and out-of-plane polarization P are absent for a flat stretched SL MX_2 (a); and a small uniform P can appear for MXY (e). A freestanding SL MX_2 (b) and MXY (f). Rippled and strained SL MX_2 (c) and (d) and MXY (g) and (h) clamped to a flat (c) and (g) or rough (d) and (h) rigid substrate. Parts (a)–(c) are reprinted from Ref. [35].

A flat single layer (SL) with chemical formula MX_2, where M is a transition metal and X is a chalcogenide is shown in Fig. 1(a). Projections of M ions are located on the middle line between projections of X ions. The inhomogeneous strain is absent in a flat SL MX_2. Since the effective (Born or Bader) charges Q of M and X ions are opposite, namely, $Q_M = -2Q_X$, the total polarization is zero. For the case of a stretched flat JC with a chemical formula XMY, the top X and bottom Y chalcogen ions are in nonequivalent conditions despite their planes being parallel [see Fig. 1(d)]. While the total charge is zero, $Q_M = -Q_X - Q_Y$, the surface-induced piezoelectric effect can induce surface dipoles. The dipoles are responsible for the nonzero total out-of-plane polarization P shown by the dashed black curve and arrows in Fig. 1(d).

A mechanically free SL MX_2 and MXY, where all X, Y, and M ion positions can spontaneously reconstruct into the rippled state with the lowest energy, are shown in Figs. 1(b) and 1(f). Since the force matrix [38] is different for the "light" X (or Y) and "heavy" M ions, the amplitudes of the X (or Y) and M ion displacements are different for the periodic ripples. Since the total effective charge is zero, the periodic displacement of X (or Y) and M ions induces the out-of-plane polarization modulation (dashed black curve and arrows) due to the flexoelectric coupling only.

The flexoelectric coupling exists for all possible symmetries [39] and geometries of the TMD and JC; hence, the effect always contributes to the total polarization, as shown in Figs. 1(b)–1(d) and 1(f)–1(h). The surface-induced piezoelectric effect contributes to the out-of-plane polarization of a SL MX_2 only for the case on nonequivalent conditions for the top and bottom chalcogen layers; that is the case of one surface being free and the other clamped to a flat rigid substrate [see Fig. 1(c)]. Since the top Y and bottom X chalcogen layers have different force matrices, the surface-induced piezoelectric effect always induces the out-of-plane polarization of a SL MXY [see Figs. 1(e)–1(g)].

Since the bottom X ions are bonded to the substrate [40] by different types of van der Waals (vdW) forces [41,42], in the case of strong adhesion [43,44] they remain almost clamped to the atomic planes of a flat (e.g., atomically smooth) substrate or to the islands of atoms of a rough (e.g., corrugated) substrate. For the case of rough substrates used in, e.g., experiments [1,24], the inhomogeneous strain can exist in the clamped sections, while the suspended sections can relax freely [see Figs. 1(d) and 1(h)]. The amplitude of the clamped atoms' vertical displacement is very small there, while a more visible change of position is possible for the middle and top ions. A significant reconstruction occurs for the ions at suspended sections, where the different amplitudes of the displacement of bottom X, middle M, and top X (or Y) ions induce the polarization (dashed black curve and arrows) due to the flexoelectric coupling in MX_2, and both the flexoelectric coupling and surface-induced piezoelectric effect in MXY.

The out-of-plane polarization component P_3 [32] of a SL TMD (or JC) shown in Figs. 1(b)–1(h) can be estimated by a continuum media approach [35], which is applicable even for ultrathin layers [23,25] and becomes quantitative for thicknesses greater than 10 lattice constants [7–9]. Within the framework of a continuum media approach [35], P_3 comprises the flexoelectric and piezoelectric contributions. The first one is proportional to the second derivatives of elastic displacement in space and time multiplied by the static and dynamic flexoelectric coefficients, respectively. The second one is proportional to the surface-induced piezoelectric coefficient multiplied by an elastic strain. So

$$P_3(\vec{x},t) \cong f_{3jkl}\frac{\partial^2 U_j(\vec{x},t)}{\partial x_k \partial x_l} - \mu_{3j}\frac{\partial^2 U_j(\vec{x},t)}{\partial t^2} + \frac{e^s_{3jk}}{t}\frac{\partial U_j(\vec{x},t)}{\partial x_k}. \tag{1}$$

Here $U_j(\vec{x})$ is the mechanical displacement of the flake, which includes spontaneous and misfit contributions, f_{ijkl} is the static flexoelectric tensor [39] determined by the microscopic properties of the material [45,46], μ_{ij} is the dynamic flexoelectric tensor [47], e^s_{ijk} is the tensor of the surface-induced piezoelectric effect [48,49] measured in picocoulombs per meter, and t is the flake thickness [50]. Einstein summation notation is used hereinafter.

It follows from the symmetry considerations that e^s_{3jk} is zero for a flat centrosymmetric MX_2 with inversion axis “3”; it was estimated approximately as −2.4 pC/m for a reconstructed SL-MoS$_2$ in the 1T' phase [15]. It is much higher ($e^s_{31} \sim 50$ pC/m) for an asymmetric JC MoSTe [28,33]. Both of these values are much smaller than in-plane components, $e^s_{1jk} \sim 300 - 500$ pC/m, estimated for MoS$_2$, MoTe$_2$, and MoSTe [15,28].

The linear partial differential equation relating the mechanical displacement $U_j(\vec{x})$ of the flake points and its elastic stress σ_{ij} has the form

$$\rho\frac{\partial^2 U_i}{\partial t^2} + \frac{\partial}{\partial x_j}\sigma_{ij}(\vec{x},t) = \mu_{ij}\frac{\partial^2 P_j}{\partial t^2} + \frac{\partial}{\partial x_i}\psi(\vec{x},t), \tag{2}$$

where ρ is the density of material and $\psi(\vec{x},t)$ is the elastic force density (with dimensionality newtons per cubic meter) in the nanoflake. The physical origin of these forces can include the atomic reconstruction of the free surface, as well as adhesion (e.g., vdW force) to the flat or corrugated substrate. Within a continuum media approach, which we use here, the force is given by a standard Lenard-Jones potential [41–44].

For the static case considered here, Eq. (1) reduces to

$$P_3(\vec{x}) \cong f_{3jkl}\frac{\partial}{\partial x_j}u_{kl}(\vec{x}) + \frac{e^s_{3jk}}{t}u_{jk}(\vec{x}), \tag{3a}$$

where $u_{kl} = (1/2)[(\partial U_k/\partial x_l) + (\partial U_l/\partial x_k)]$ is an elastic strain tensor. The coupling between the stress σ_{ij} and strain u_{kl} is given by the generalized Hooke’s law [51],

$$\sigma_{ij} = c_{ijkl}u_{kl} + F_{ijmn}\frac{\partial P_m}{\partial x_n} + h^s_{3ij}P_3 \approx c_{ijkl}u_{kl} + O[f^2_{3ij}, (h^s_{3ij})^2], \tag{3b}$$

where c_{ijkl} is the tensor of elastic stiffness, F_{ijmn} is a flexoelectric tensor (in volts), and h^s_{mij} is a surface-induced piezoelectric stress tensor (in volts), which is absent for a centrosymmetric MX_2 and present for Janus MXY. The approximate equality is the decoupling approximation, valid for small flexoelectric and surface piezoelectric effects, which are indeed small in the considered case.

Using the decoupling approximation in Eq. (3b), Eq. (2) yields the Lame equation

$$c_{ijkl}\frac{\partial^2 U_k(\vec{x})}{\partial x_j\, \partial x_l} = \frac{\partial}{\partial x_i}\psi(\vec{x} - \vec{x}_s), \tag{3c}$$

where $\vec{x}_s$ is the corrugation profile of a rough substrate (see Fig. 2).

To solve Eq. (3c), we need to define the adhesion force $\psi(\vec{x})$ between the layers of X, M, and/or Y atoms, and an atomically flat or corrugated substrate. Here we use the assumption that the constitutive parts of the vdW forces [41] corresponding to dipole-dipole interactions, and dispersive-dipole interactions and London dispersive forces, determine the atomic repulsion at ultrasmall distances, and their attraction at greater distances.

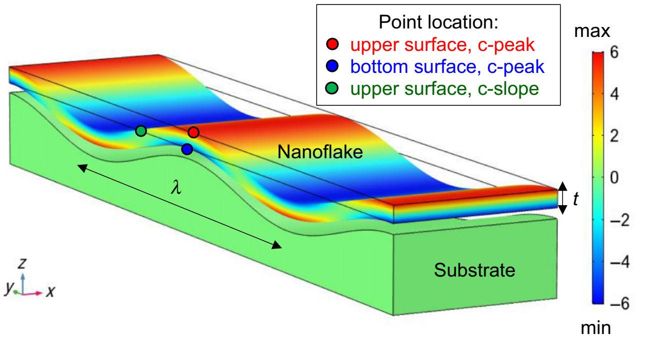

FIG. 2. Considered geometry. A nanoflake of TMD is placed on a corrugated substrate. The scale on the right schematically shows the variation of electric polarization, induced by the flexoelectric effect, and electric conductivity, induced by inhomogeneous elastic strain via the deformation potential. The red and blue circles located at the upper and bottom surfaces of the nanoflake at the peak of the substrate corrugation, are abbreviated as “c-peak”. The green circle located on the corrugation slope is abbreviated as “c-slope”. Further we analyze the behavior of the physical properties in these three characteristic points of the nanoflake surface.

TABLE I. Material constants for LD MX_2 and MXY, and rough substrate.

Material	LD $\mathrm{MoS_2}$	LD $\mathrm{MoTe_2}$	LD or SL MoSTe
Symmetry/phase[a]	6/mmm, $2H$ or $1H$	6/mmm, $2H$ or $1H$	3m, $1H$
Lattice constants (nm)	$c = 1.1$, $a = 0.32$	$c = 1.4$, $a = 0.35$	$c = 1.3$, $a = b = 0.34$
Elastic stiffness tensor (GPa)	$c_{11} = 134.3$, $c_{12} = 33.3$	$c_{11} = 139.0$, $c_{12} = 71.0$ (for $v > 0$)	$c_{11} = 116$, $c_{12} = 28$
Young's modulus E (GPa)	250 Ref. [53] 136 Ref. [54]	(90–110) Ref. [55] we use 100	105
Poisson ratio ν	−0.07 [56]	0.34 [55] (but $v = -0.08$ from [56])	0.24–0.30 [57]
Effective piezo-response tensor d^{eff}_{ijk} (pm/V)	$d^{\mathrm{eff}}_{11} = 5.76$ [15] $d^{\mathrm{eff}}_{31} = -0.018$ [15]	$d^{\mathrm{eff}}_{33} \approx 3$ [24] $d^{\mathrm{eff}}_{11} = 9.13$ [58] $d^{\mathrm{eff}}_{11} = 7.39$ [27]	$d^{\mathrm{eff}}_{11} = 5.1$ [57] $d^{\mathrm{eff}}_{31} = 0.4$ [57]
Surface-induced out-of-plane piezoelectric coefficients e^s_{3jk} (pC/m)	$e^s_{31} = 0$ $e^s_{33} = 0$	$e^s_{31} = 0$ $e^s_{33} = 0$	$e^s_{31} = 50$ $\lvert e^s_{33}\rvert < 5$ [28,33,57]
Flexoelectric effect tensor f_{ijkl} (nC/m) Ref. [59]	$f_{13} = 4.44$ $f_{13} = 4.44$	$f_{13} = 9.50$ $f_{11} = 9.50$	unknown, set equal to $f_{13} = f_{33} = 6.47$
Deformation potential tensor Σ_{ij} (eV)	$\Sigma_h = 5.61$ [28] $\Sigma_e = -11.14$ [28] $\Sigma_g = -(13.8–17)$ Ref. [22]	$\Sigma_h = 4.2$ (this work) $\Sigma_e = -7$ (this work) $\Sigma_g = -(3.8–11)$ Ref. [22]	unknown, set equal to $\Sigma_h = -5$ (this work) $\Sigma_e = -7$ (this work)
Substrate characteristics	Adhesive stiffness varies in the range $S_A = (2–20)$ GPa, adhesion repulsive separation $\delta h_0 = 1.1$ nm. Substrate material is gold, graphite, mica, and silica oxide. The average period of corrugation $\lambda = 0.5$ μm, the amplitude A of substrate roughness from 0 to 11 nm. Substrate thickness is 200–500 nm		

[a] We consider LD MoX_2 to be in the semiconducting H phase (typically $2H$) under normal conditions. MXY monolayers lack the reflection symmetry and are neither $2H$ nor $1H$ [5].

In this approximation, the adhesion force (per unit volume, in joules per cubic meter) between the flake and substrate can be approximated by a power law attraction with a prefactor-contact adhesive stiffness S_A at distances $|\vec{x} - \vec{x}_s| > \delta h_0$, and strong repulsion at distances $|\vec{x} - \vec{x}_s| < \delta h_0$ (see also Appendix A in the Supplemental Material [52]). The force characteristics, namely adhesive stiffness and repulsive separation, should be implemented in the software used for FEM.

Using FEM, performed in COMSOL Multiphysics software (see details in Appendix B in the Supplemental Material [52]), we analyze the scenario in which TMD nanoflakes are placed on a rough substrate with an ideal 1D sinusoidal corrugation profile $\vec{x}_s = \{0, 0, A\cos[(2\pi/\lambda)x_1]\}$ corresponding to the case of perfect 1D ripples. Thus, we consider an ideal 2D problem, when all physical variables are regarded as being dependent on the in-plane coordinate x_1 and out-of-plane coordinate x_3, but are independent on the other in-plane coordinate x_2.

For sufficiently strong adhesion forces, the flake displacement, strain, strain gradient, and out-of-plane electric polarization [given by Eq. (1)] are modulated by the corrugation profile, being maximal at the corrugation peaks and minimal in the valleys (see Fig. 2). Material parameters of several MX_2, MXY, and substrate characteristics used in FEM are listed in Table I. All calculations are performed at room temperature $T = 300$ K.

The inhomogeneous elastic strain should induce changes in the electron and hole charge densities, $n(\vec{x})$ and $p(\vec{x})$, in the flake due to the coupling with band structure via a deformation potential

$$\frac{n(\vec{x})}{n_0} = \frac{1}{n_0}\int_0^\infty \frac{g_n(\varepsilon)d\varepsilon}{1 + \exp\{[\varepsilon - E_F + E_c + \Sigma^e_{ij}u_{ij}(\vec{x}) - e\varphi]/k_BT\}} \sim \exp\left[-\frac{\Sigma^e_{ij}u_{ij}(\vec{x}) - e\varphi}{k_BT}\right], \tag{4a}$$

$$\frac{p(\vec{x})}{p_0} = \frac{1}{p_0}\int_0^\infty \frac{g_p(\varepsilon)d\varepsilon}{1 + \exp\{[-\varepsilon + E_F - E_V + \Sigma^h_{ij}u_{ij}(\vec{x}) + e\varphi]/k_BT\}} \sim \exp\left[-\frac{\Sigma^h_{ij}u_{ij}(\vec{x}) + e\varphi}{k_BT}\right], \tag{4b}$$

where

$$n_0 = \int_0^\infty \frac{g_n(\varepsilon)d\varepsilon}{1+\exp[(\varepsilon - E_F + E_c)/k_B T]}$$

and

$$p_0 = \int_0^\infty \frac{g_p(\varepsilon)d\varepsilon}{1+\exp[(-\varepsilon + E_F - E_V)/k_B T]}$$

are the electron and hole concentrations in the unstrained nanomaterial, $g_n(\varepsilon)$ and $g_p(\varepsilon)$ are the densities of electron and hole states, E_F is the Fermi energy, $k_B = 1.380\,710^{-23}$ J/K is the Boltzmann constant, and Σ_{ij}^{e} and Σ_{ij}^{h} are the deformation potential tensors for electrons and holes, respectively. The values $\Sigma_{ij}^{e,h}$ are the fitting parameters of the continuum model; they should be either taken from the first-principles calculations or estimated from experiments. The values of $\Sigma_{ij}^{e,h}$ are listed in Table I for several MX_2. The proportionality in Eqs. (4) is valid for the Boltzmann-Plank-Nernst statistics of nondegenerate carriers. Since the band gap of MX_2 and MXY is about 1–2 eV, we can expect that rippled MX_2 and MXY should become conductive once the spontaneous strain value exceeds several percent, which makes the product $|\Sigma_{ij}^{e,h} u_{ij}|$ much higher than the thermal energy $k_B T$.

III. CORRELATION BETWEEN POLAR AND ELECTRONIC PROPERTIES OF MX_2 AND MXY NANOFLAKES

Spatial distributions and profiles of elastic strain, its gradient, polarization, and charge density of the TMD and JC nanoflakes are shown in Figs. 3–7. Additional details are shown in Figs. S2–S5 in Appendix B of the Supplemental Material [52] and briefly described here. One period of the substrate corrugation profile $\vec{x}_s = \{0,\ 0,\ A\cos[(2\pi/\lambda)x_1]\}$ is shown in all these figures, and the unambiguous correlations between the maximal or minimal values of the strain, strain gradient, polarization, and charge density are clearly seen in the corrugation period.

The cross sections of the bending-induced elastic displacement, strain components, out-of-plane polarization, and carrier density distributions are shown in Figs. 3(a)–3(f) for MoS_2, and in Figs. 3(g)–3(l) for $MoTe_2$ nanoflakes of the same thickness (approximately 28 nm) on a thick rough substrate. It is seen that the nanoflake displacement, strain, strain gradient, out-of-plane polarization and charge density are modulated by the corrugation profile, being maximal at the corrugation peaks, zero on the slopes, and minimal in the valleys. Furthermore, the relative increase of the electron density for MoS_2 (more than 10 times) is much higher than that for $MoTe_2$ (less than

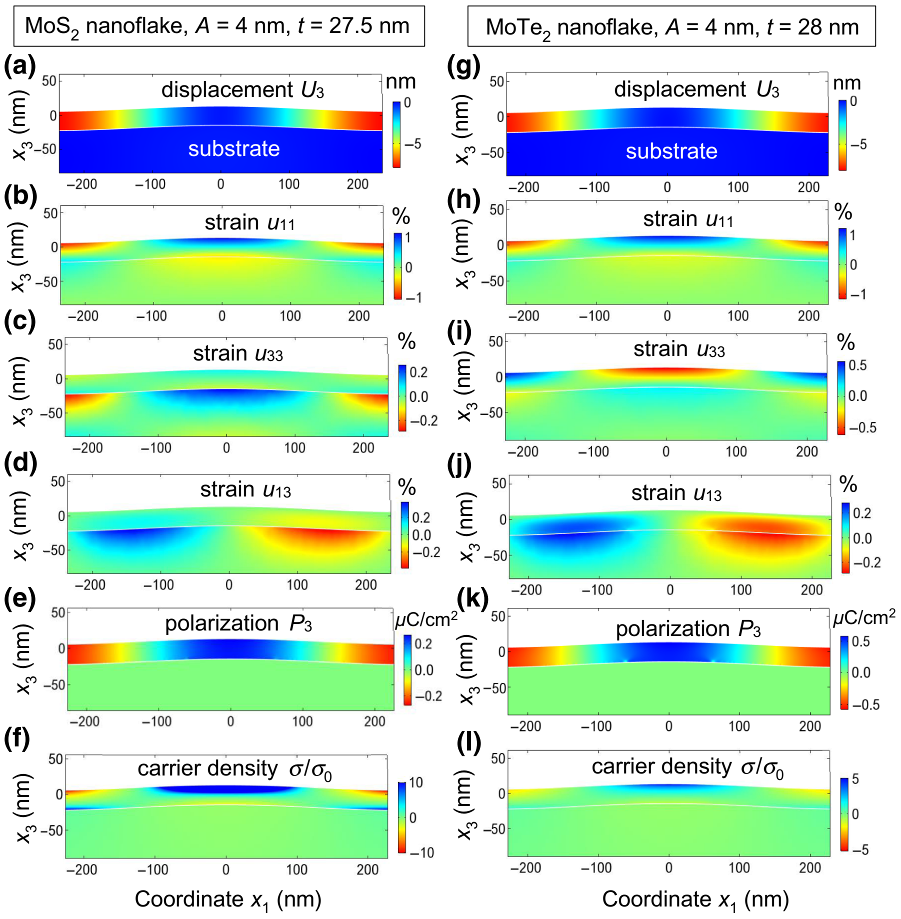

FIG. 3. Distributions of polar and electronic properties in MoS_2 (a)–(f) and $MoTe_2$ (g)–(l) nanoflakes. Bending-induced elastic displacement (a) and (g), strain tensor components (b)–(d) and (h)–(j), out-of-plane polarization (e) and (k), and relative carrier density σ/σ_0 (f) and (l) in the cross section of a MoS_2 (a)–(f) and $MoTe_2$ (g)–(l) nanoflake of thickness $t \approx 28$ nm, placed on a 200-nm-thick rough substrate. The amplitude A of the substrate corrugation is 4 nm, and the average period of the corrugation is $\lambda = 0.5\ \mu$m. MoS_2, $MoTe_2$, and substrate parameters are listed in Table I.

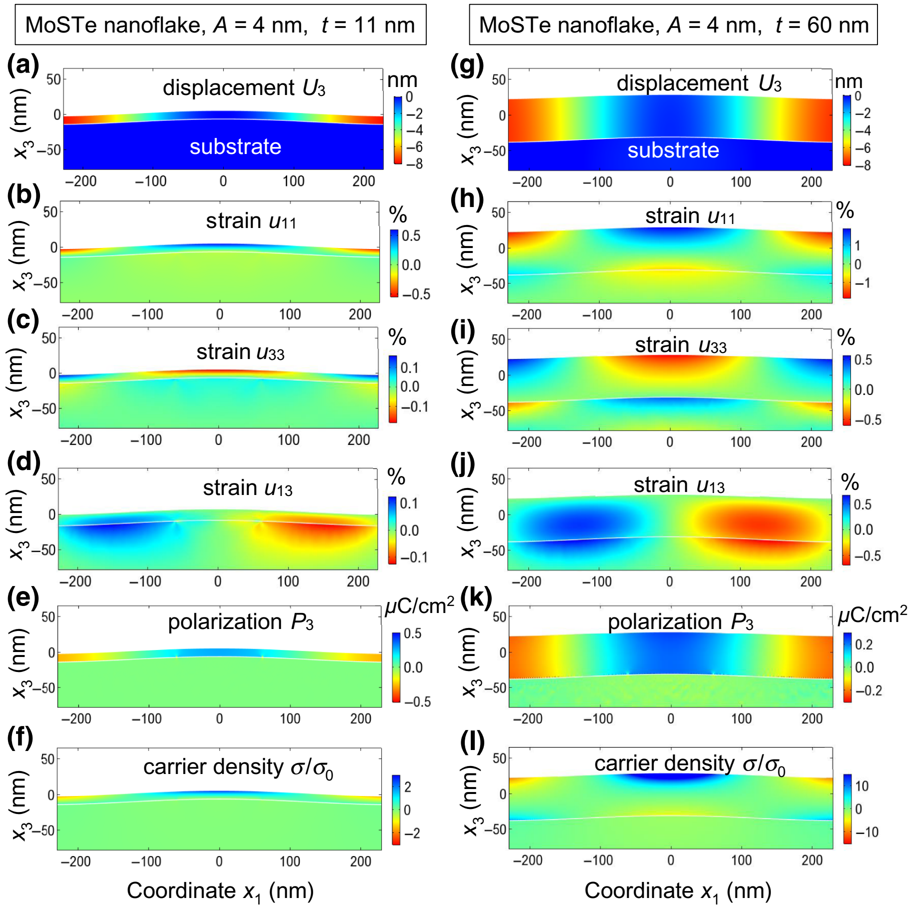

FIG. 4. Distributions polar and electronic properties in MoSTe nanoflakes with thickness 11 nm (a)–(f) and 60 nm (g)–(l). Bending-induced elastic displacement (a) and (g), strain tensor components u_{11}, u_{33} and u_{13} (b)–(d) and (h)–(j), out-of-plane polarization (e) and (k), and relative carrier density σ/σ_0 (f) and (l) in the cross section of the nanoflake placed on a thick rough substrate. The amplitude A of the substrate corrugation is 4 nm, and the average period of the corrugation is $\lambda = 0.5$ μm. MoSTe and substrate parameters are listed in Table I.

5 times) [compare Figs. 3(f) and 3(l)]. Regions enriched by holes (more than 10 times) exist in MoS$_2$ nanoflakes. Hence, the appearance of p-n junctions between the n-type and p-type regions is possible in MX_2 nanoflakes, similar to the case of graphene-on-ferroelectric nanostructures [11, 12]. The distinct feature of MX_2 nanoflakes-on-corrugated substrate is that the width, diffuseness, or sharpness of the p-n junctions can be controlled by the flake thickness, t, and by the relative substrate corrugation, A/λ.

The cross sections of bending-induced elastic displacement, strain components, and out-of-plane polarization for ultrathin MoSTe nanoflakes [e.g., 10 layers or thinner, see Figs. 4(a)–4(f)] look only a bit different from those of thicker MX_2 nanoflakes (shown in Figs. 3) due to the thickness effect. When the MoSTe nanoflake thickness increases [see Figs. 4(a)–4(f)], the overall picture looks like an "average" of the MoS$_2$ and MoTe$_2$ nanoflakes shown in Figs. 3. Note the possible appearance of the p-n junctions between the n-type and p-type regions in MXY nanoflakes, similar to the case of MX_2 nanoflakes.

The influence of the surface-induced piezoelectric effect (present in MoSTe and absent for 1H and 2H-MoX_2) appears to be too small to affect significantly the polar and electronic property distributions shown in Fig. 4. Hence, even for the case of a JC MoSTe, the dominant part of the polarization is the flexoelectric polarization. This conclusion is clearly seen from a comparison of the scales in Figs. S6(a) and S6(b) of the Supplemental Material [52], where the magnitude of the piezoelectric polarization is about 2 nC/cm^2, while the magnitude of the flexoelectric polarization is two orders higher, at about 0.4 μC/cm^2 for flake thicknesses of approximately 4–20 nm. Furthermore, the contribution of the surface-induced piezoelectric effect decreases with the flake thickness according to Eq. (3) [compare brown and black curves in Fig. S6(a)].

The curves in Fig. 5 are calculated for different amplitudes of substrate roughness $A = 0 - 11$ nm and approximately the same thickness of approximately 11 nm (corresponding to the range of 8 to 10 layers) of MoS$_2$, MoTe$_2$ and MoSTe nanoflakes. The bending-induced out-of-plane flexoelectric polarization and relative electron density monotonically increase with increasing A. Furthermore, the relative increase in the electron density for MoS$_2$ ($>10^3$ times) is much higher than that for MoTe$_2$ (>10 times), and also than that for MoSTe (>20 times) [compare Figs. 5(b), 5(d) and 5(f)]. The difference is related to the significantly higher electronic deformation potential of MoS$_2$ (see Table I). The profiles of the out-of-plane flexoelectric polarization, which is proportional to the strain gradient, demonstrate visible deviations from the

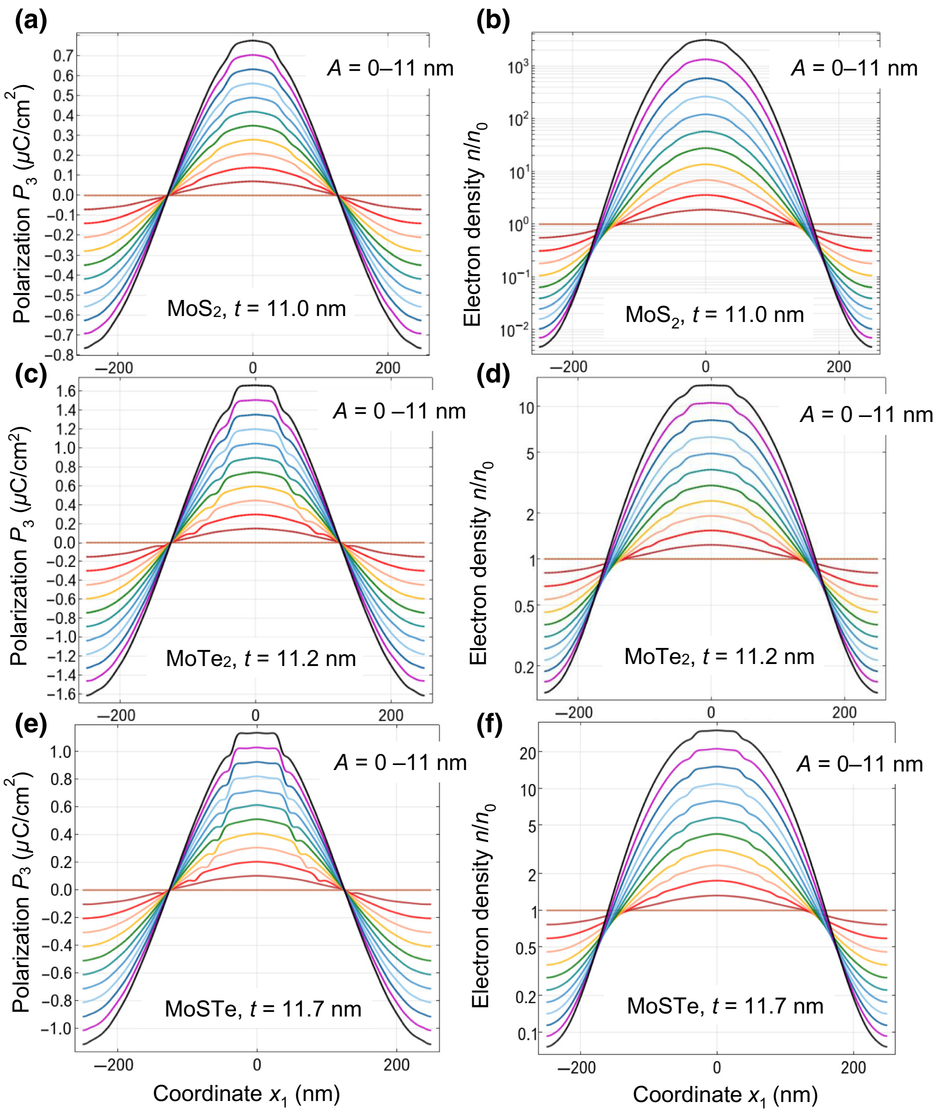

FIG. 5. Profiles of polar and electronic properties of MoS_2, $MoTe_2$, and MoSTe nanoflakes. Bending-induced out-of-plane polarization (a), (c) and (e), and relative electron density (b), (d) and (f) at the upper surface of the nanoflake with thickness $t \approx 11$ nm, which is placed on a thick rough substrate. Twelve curves correspond to the different values of corrugation amplitude $A = 0, 1, 2, 3, 4, \ldots 11$ nm (from $A = 0$ nm, the brown line, to $A = 11$ nm, the top black curve). Nanoflakes and substrate parameters are listed in Table I.

sinusoidal profile of the substrate, since the top regions of the 10 curves plotted for $A = 2 - 11$ nm have two symmetric indentations, whose height increases and locations become closer to the peak $x_1 = 0$ with increasing A [see Figs. 5(a), 5(c) and 5(e)].

The bending dependence of polar and electronic properties of MoS_2 and $MoTe_2$ nanoflakes are shown in Figs. 6(a)–6(d). The bending-induced elastic strain and strain gradient, out-of-plane flexoelectric polarization, and relative electron density of the nanoflakes monotonically increase with the increase of corrugation amplitude A. The increase of the strain and electron density is linear at small $A < 5$ nm and becomes super-linear at $A > 10$ nm; it is much higher at the upper surface of the nanoflake in comparison with its bottom surface [compare the red and brown and the blue and black circles in Figs. 6(a) and 6(d)]. In contrast, the strain gradient and flexoelectric polarization, which increase linearly with increasing amplitude A, are almost the same at the upper and bottom surfaces [compare the red and brown and the blue and black circles in Figs. 6(b) and 6(c)]. There are qualitative similarities, but quantitative differences between MoS_2 and $MoTe_2$ nanoflakes, which are most pronounced for polarization (2 μC/cm^2 vs 4 μC/cm^2), and relative electron density ($\gg 10^3$ vs 10^2) maximal values.

The thickness dependence of polar and electronic properties of MoS_2 and $MoTe_2$ nanoflakes are shown in Fig. 7. The blue, black, red, and brown circles, which correspond to the corrugation peaks, where the strain and strain gradient are maximal, show the maximal increase of the flexoelectric polarization, and electron or hole densities. The green and purple circles, which correspond to the corrugation slope, where the strain and strain gradient are absent, show almost zero polarization and no increase in the electron or hole density. Most importantly, there is a pronounced maximum in the thickness dependences of the elastic strain, electron conductivity, and hole conductivity of MoS_2 and $MoTe_2$ nanoflakes placed on a rough

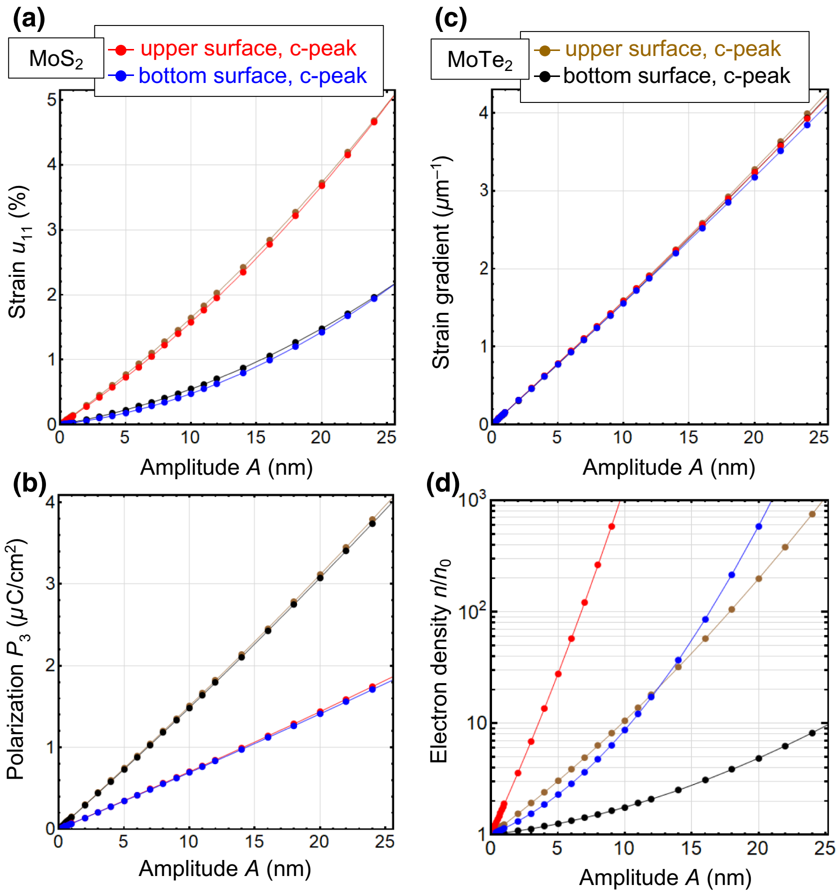

FIG. 6. Bending dependence of polar and electronic properties of MoS$_2$ (red and blue circles) and MoTe$_2$ (brown and black circles) nanoflakes. The bending-induced elastic strain (a) and strain gradient (b), out-of-plane polarization (c), and relative electron density (d) of a nanoflake with the corrugation amplitude A of the rough substrate. The quantities (a)–(d) are shown at the upper (red and brown circles) and bottom (blue and black circles) surfaces of the nanoflake, which are placed at the peaks of the substrate corrugation (abbreviated as c-peak, see Fig. 2). The flake thickness is 11 nm, the average period of corrugation $\lambda = 0.5$ μm. MoX_2 and substrate parameters are listed in Table I.

substrate. The optimal thickness is corrugation dependent, and it is 75 nm for MoS$_2$ and 80 nm MoTe$_2$ nanoflakes in the case of a 4 nm corrugation height. The result opens the way for geometry optimization of a nanoflake placed on a substrate with a sinusoidal corrugation profile.

It is notable that corresponding bending and thickness dependence curves for MoSTe nanoflakes lie between those for MoS$_2$ and MoTe$_2$ nanoflakes, as anticipated from Fig. 5. They are not shown in Figs. 6 and 7, since the “mixture of curves” appears when we add two or three more curves.

Analysis of the FEM results obtained for the different flake thicknesses (varying from 10 to 300 nm) and corrugation depth (varying from 0 to 25 nm), allows the corroboration of the flexoelectric nature of the out-of-plane polarization [24] and establishes the unambiguous correlation between the polarization and n-type (or p-type) static conductivity modulation. The modulation is caused by inhomogeneous elastic strains coupled with deformation potential, and strain gradients, which evolve in TMD nanoflakes due to the adhesion between the flake surface and corrugated substrate.

The obtained results can be useful for the elaboration of nanoscale straintronic devices based on the MX_2 and MXY nanoflakes bended by a corrugated substrate. Principal schemes of diodes and bipolar transistors are presented in Fig. 8, where the bending profile of a semiconducting nanoflake controls the sharpness of p-n junctions between the regions with n-type (electron) and p-type (hole) conductivity. To create real prototypes of devices, one should take into account possible disadvantages related to the “doubled” geometry of the obtained p-n junctions. Namely, we calculate more faint “extra” p-regions located at the flake-substrate boundary below the top n-regions, and extra n-regions located at the flake-substrate boundary below the top p-regions. However, for a specific device architecture the doubled geometry in complexes with very high mechanical stability and flexibility of the nanoflakes-on-substrate may become a benefit.

To resume the section, the considered 2D problem can describe quantitatively the real situation in which a nanoflake is placed on a highly oriented substrate with an almost perfect 1D corrugation profile obtained by, e.g., self-assembling or self-organization. In this case, we expect that it is possible to reach high conductivity, which is strongly correlated with relatively high flexoelectric polarization, by selecting the optimal ratio between the corrugation period λ, its amplitude A and nanoflake thickness t.

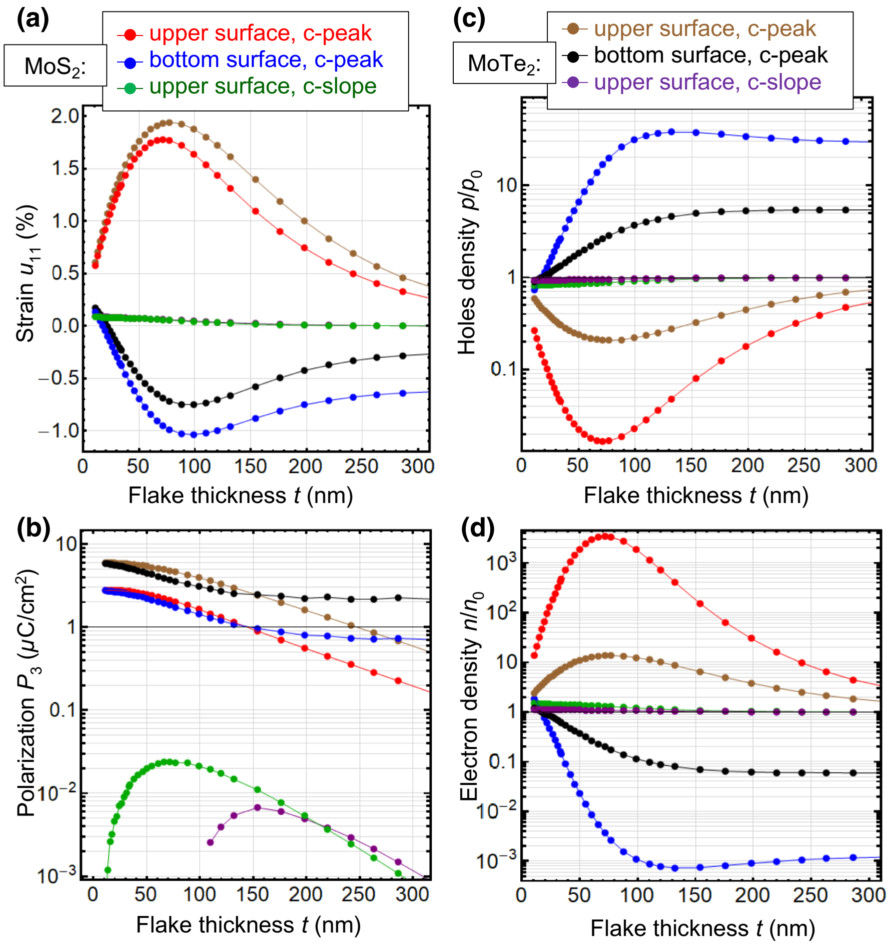

FIG. 7. Thickness dependence of polar and electronic properties of MoS$_2$ (red, green, and blue circles) and MoTe$_2$ (brown, purple, and black circles) nanoflakes. The bending-induced elastic strain (a), out-of-plane polarization (b), hole density (c), and electron density (d) with the thickness of a nanoflake placed on a rough substrate. The quantities (a)–(d) are shown at the upper (red and brown circles) and bottom (blue and black circles) surfaces of the nanoflake, which are placed at the peaks of the substrate corrugation (abbreviated as c-peak, see Fig. 2). Green and purple circles correspond to the corrugation slope (abbreviated as c-slope, see Fig. 2). The amplitude of substrate corrugation $A = 4$ nm, the average period of the corrugation $\lambda = 0.5$ μm. MoX_2 and substrate parameters are listed in Table I.

However, the real ripples cannot be completely 1D, and there can also be corrugation in other directions. FEM for the case of a substrate with a 2D corrugation profile (and especially with a random 3D corrugation profile) is a significantly more complex task requiring much more computer time and memory resources, which increase with the flake thickness. Our preliminary FEM results confirm the strong correlation between the enhanced conductivity of the nanoflake and its flexoelectric polarization at the corrugation peaks. The enhancement is more pronounced for a higher ratio of peak height to peak width, which is an analog of the A/λ ratio in the 1D case, but the effect of carrier density inversion at the valleys is rather weak or not observable. This is related to the strain concentration at the localized corrugation peaks and their relaxation in the valleys.

Overall, FEM results for 2D and 3D corrugated substrates are not obvious and require a separate study. Moreover, due to the effect of complexity for the most realistic case of the substrate with a random 3D corrugation, the procedure of optimizing the nanoflakes' polar and conductive properties is much more complex in comparison with the flakes on 1D corrugated substrates considered in this work.

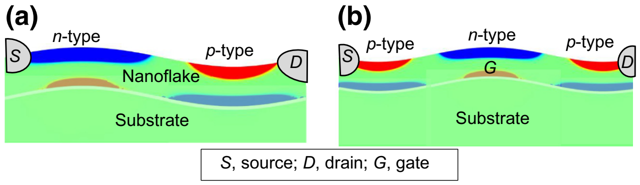

FIG. 8. Principal schemes of a diode (a) and bipolar transistor (b) based on a 13-nm-thick MoSTe nanoflake bended by a corrugated substrate. The regions with *n*-type (electron) and *p*-type (hole) conductivity are shown.

IV. COMPARISON WITH EXPERIMENT

Note that the calculated strain-induced enhancement of carrier density is regulated by the components Σ_{ij} of the deformation potential tensor, which are the fitting parameters within the continuum media approach used in FEM. An appropriate choice of the Σ_{ij} (either from DFT calculations or from experiment) can lead to enhancements of 5–10^4 times. This tunability makes FEM complementary to the results of Duerloo *et al.* [16], who predicted a strain-induced phase transition from a semiconducting 2H to a metallic 1T' phase in various MX_2. Later on, Song *et al.* [60] observed a room temperature semiconductor-metal transition in thin $MoTe_2$ films induced by a homogeneous tensile strain of 0.2%.

Our FEM results, obtained for the case of inhomogeneous periodic bending of MX_2 nanoflakes, better agrees with the experiment of Kang *et al.* [24], who established the correlations between atomic force microscopy (AFM) topography and conductive atomic force microscopy (cAFM) conductive spots in $MoTe_2$ nanoflakes placed on a gold corrugated substrate. Kang *et al.* observed multiple conductive spots located at the corrugation peaks [see, e.g., parts (a), (b) and (e) in Fig. S5 in the Supplemental Material of Ref. [24]]. The difference in the negative cAFM contrast at the corrugation peaks (−15 nA) in comparison with the positive cAFM contrast at the valleys (+4 nA) was about 4.75 times, which is very close to the ratio of maximal:minimal carrier density (about 5 times) shown in Fig. 3(l) and Fig. 9.

Figure 9 compares the experimental results [24] and FEM results obtained in this work. The left side of the figure shows the surface topography (top image) and cAFM contrast (bottom image) of $MoTe_2$ nanoflake with a thickness of 10 nm measured by Kang *et al.* [24]. The right side shows the corrugation (top image) and relative carrier density σ/σ_0 (bottom image) color maps calculated by FEM for a 10-nm-thick $MoTe_2$ nanoflake placed on a rough substrate with several well-separated corrugation peaks. We note that each peak has a Gaussian distribution of corrugation with its own height, maximum position, and dispersion, whose values are random, but are of the same order as in the experiment [24]. Assuming that the carrier density is proportional to C-AFM contrast in the simplest case, Fig. 9 demonstrates a semiquantitative agreement between our simulations and experiment [24]. It is notable that both the experimentally measured topography peaks and calculated corrugation distribution look much more diffuse, often merging together, in comparison with the well-separated measured cAFM contrast and calculated carrier density spots. Since the carrier density $\sigma(\vec{x})$ exponentially depends on the flake strain $u_{ij}(\vec{x})$ in accordance with Eq. (4), $(\sigma(\vec{x})/\sigma_0) \sim \exp\{-[\Sigma_{ij} u_{ij}(\vec{x})/k_B T]\}$, and the flake strain is a rather linear function of the substrate corrugation, the carrier density should be a sharp (e.g., exponential) function of the corrugation. So, we can conclude that our simulations confirm the fact that the enhancement of local carrier density (and so the local conductivity) is pronounced at the corrugation peaks, but the effect of the carrier density inversion at the valleys and slopes is relatively weak. This is related to the strain concentration at the corrugation peaks and their relaxation in the valleys. The enhancement at the peaks is inherent for a 3D problem, while 1D corrugation can lead to the inversion effect in the valleys (compare Figs. 3 and 9).

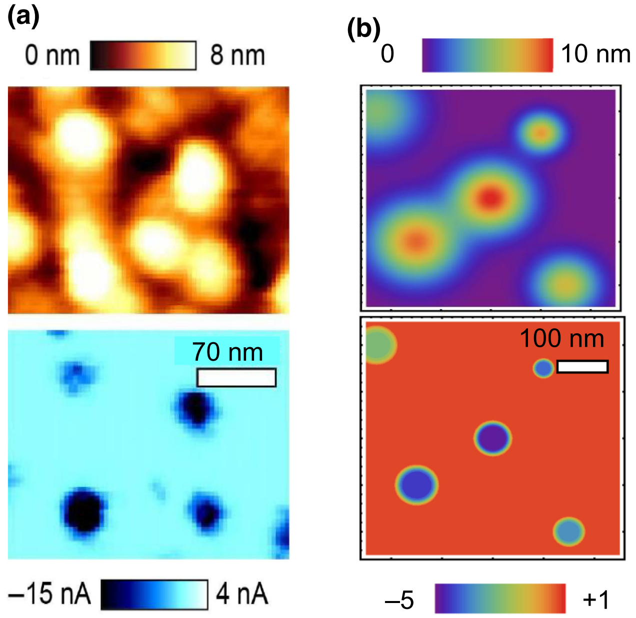

FIG. 9. (a) Surface topography (top image) and cAFM contrast (bottom image) of a 10-nm-thick $MoTe_2$ nanoflake obtained for the dc voltage –0.25 V applied to the tip. Reprinted with permission from [S. Kang, S. Jeon, S. Kim, D. Seol, H. Yang, J. Lee, Y. Kim, ACS Appl. Mater. Interfaces 10 (2018) 27424–27431]. Copyright (2018) ACS Publications. (b) Corrugation (top image) and relative carrier density σ/σ_0 (bottom image) color maps calculated by FEM for a 10-nm-thick $MoTe_2$ nanoflake placed on a rough substrate with several well-separated corrugation peaks.

To verify the theoretical results for MoS_2 nanoflakes, their structure is examined by scanning tunneling microscopy (STM) in nonvacuum conditions (see details in Appendix C of the Supplemental Material [52]). As substrates, we use highly ordered pyrolytic graphite (HOPG) and Au(111) on mica. STM images, shown in Figs. S7–S8, reveal MoS_2 nanoflakes of different shapes and sizes. Typical local volt-ampere characteristics (*I*-*V* curves) measured at the same point of a nanoflake are shown in Fig. 10 (more *I*-*V* curves are shown in Figs. S7–S8).

The tunneling current is almost absent if the voltage magnitude is less than 1 V for the HOPG substrate or less than 0.5 V for the Au(111) substrate. The difference in the "opening" voltages of the *I*-*V* curves originates from the difference in substrate conductivity and surface properties. Since neither substrate contains any specially prepared corrugations, the current is absent for a strain-free nanoflake placed in a small electric field. A strong local field appearing under the bias voltage increase causes local bending and deformation of the flake due to the electrostriction and piezoelectric mechanisms. Furthermore, the strained region of the flake can become conductive and lead to the opening of the *I*-*V* curve.

The significant variability in the *I*-*V* curves' opening scenarios and the typical jumps on the curves, which appear at an applied voltage of magnitude greater than 0.5–1 V, indicate the randomness of a tunneling current

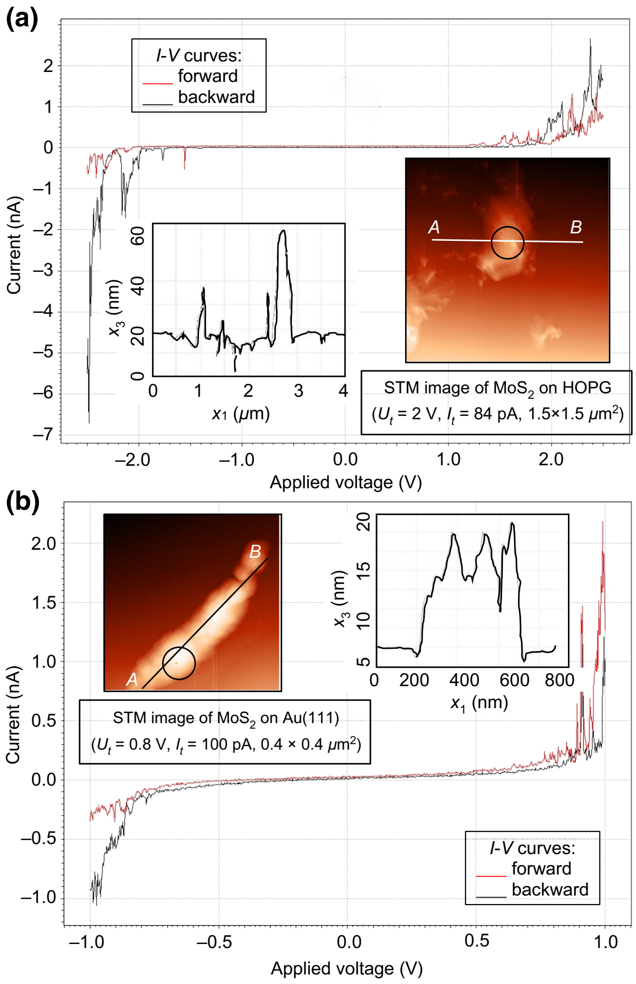

FIG. 10. Local volt-ampere characteristics of MoS_2 nanoflakes on (a) HOPG and (b) Au(111) substrates measured by STM. Left inset in the plot (a) and right inset in the plot (b) are the surface topography along the direction AB. Right inset in the plot (a) and left inset in the plot (b) are the STM images of MoS_2 nanoflakes on HOPG and Au(111) substrates, respectively. Local volt-ampere characteristics were measured in the points marked by a circle with a central yellow and red dot in the insets.

path associated with the strong local inhomogeneity of electroconductivity near the surface of MoS_2 nanoflakes, which is most likely caused by the shape changes of the nanoflakes and by the evolution of local electric fields under the current flow. In fact, the strong local inhomogeneity of the MoS_2 nanoflake conductivity can be determined by the bending of its surface in accordance with FEM results presented in this work. Hence, the STM results indirectly indicate a significant dependence of free carrier concentration in MoS_2 nanoflakes on their bending and strain gradient. The quantitative description of these results requires theoretical calculations of local electric fields coupled to elastic strains for different substrates and nanoflake shapes and sizes. This task will be performed in near future.

V. SUMMARY

Using FEM, we calculate the elastic and electric fields, out-of-plane electric polarization, and free charge density for a TMD nanoflake placed on a rough substrate with a sinusoidal profile of corrugation principal component. Analysis of FEM results obtained for different flake thicknesses (varying from 10 to 300 nm) and corrugation depths (varying from 0 to 25 nm) allows corroboration of the flexoelectric nature of the out-of-plane polarization and establishes the unambiguous correlation between the polarization and static conductivity modulation. We consider that the modulation is caused by inhomogeneous elastic strains coupled with deformation potential, and strain gradients, which evolve in the TMD nanoflake due to the adhesion between the flake surface and the corrugated substrate.

We reveal a pronounced maximum in the thickness dependences of the electron and hole conductivity of MoX_2 and MXY nanoflakes placed on a substrate with a sinusoidal corrugation. Namely, the conductivity is maximal for 75–80-nm-thick flakes placed on a rough substrate with a 4 nm corrugation height. This result opens the way for the optimization of the nanoflake geometry to significantly improve their polar and electronic properties, necessary for advanced applications in nanoelectronics and memory devices. Specifically, the obtained results can be useful for elaboration of nanoscale straintronic devices based on bended MX_2 and MXY nanoflakes, such as diodes and bipolar transistors with a bending-controllable width of p-n junctions.

ACKNOWLEDGEMENTS

This effort (S.V.K.) is based upon work (theory) supported by the US Department of Energy (DOE), Office of Science, Basic Energy Sciences (BES), Materials Sciences and Engineering Division and was performed at the Oak Ridge National Laboratory's Center for Nanophase Materials Sciences (CNMS), a US Department of Energy, Office of Science User Facility. This work (Y.K.) was supported by the Basic Science Research Program through the National Research Foundation of Korea (NRF) funded by the Ministry of Education (No. 2019R1A6A1A03033215). A.N.M, H.V.S., Y.Y.L., and G.I.D. work has received funding from the National Research Foundation of Ukraine (Grant application 2020.02/0027). A.N.M., Y.Y.L., and G.I.D. acknowledges multiple stimulating discussions with Prof. A.A. Marchenko (IP NASU).

A.N.M., Y.K., and S.V.K. generated the research idea. A.N.M. evolved the theoretical model, stated the problem, interpreted numerical results obtained by E.A.E. and H.V.S., and jointly with Y.K. and S.V.K., wrote the manuscript draft. Y.Y.L. performed STM measurements. G.I.D., Y.K., and S.V.K. worked on the results, discussion, and manuscript improvement.

[1] S. Kang, S. Kim, S. Jeon, W.-S. Jang, D. Seol, Y.-M. Kim, J. Lee, H. Yang, and Y. Kim, Atomic-scale symmetry breaking for out-of-plane piezoelectricity in two-dimensional transition metal dichalcogenides, Nano Energy **58**, 57 (2019).

[2] R. Grasset, Y. Gallais, A. Sacuto, M. Cazayous, S. Mañas-Valero, E. Coronado, and M.-A. Méasson, Pressure-Induced Collapse of the Charge Density Wave and Higgs Mode Visibility in $2H-TaS_2$, Phys. Rev. Lett. **122**, 127001 (2019).

[3] C. J. Butler, H.-H. Yang, J.-Y. Hong, S.-H. Hsu, R. Sankar, C.-I. Lu, H.-Y. Lu, K.-H. O. Yang, H.-W. Shiu, C.-H. Chen, C.-C. Kaun, G.-J. Shu, F.-C. Chou, and M.-T. Lin, Mapping polarization induced surface band bending on the Rashba semiconductor BiTeI, Nat. Commun. **5**, 4066 (2014).

[4] Y. Qi, W. Shi, P. G. Naumov, N. Kumar, R. Sankar, W. Schnelle, C. Shekhar, Fang-C. Chou, C. Felser, B. Yan, and S. A. Medvedev, Topological quantum phase transition and superconductivity induced by pressure in the bismuth tellurohalide BiTeI, Adv. Mater. **29**, 1605965 (2017).

[5] L. Dong, J. Lou, and V. B. Shenoy, Large in-plane and vertical piezoelectricity in Janus transition metal dichalchogenides, ACS Nano **11**, 8242 (2017).

[6] E. A. Eliseev, A. N. Morozovska, and M. V. Strikha, Strain Engineering of Ferromagnetic-Graphene-Ferroelectric Nanostructures, Phys. Rev. Appl. **14**, 024081 (2020).

[7] A. A. Bukharaev, A. Zvezdin, A. Pyatakov, and Yu. Fetisov, Straintronics: A new trend in micro-, nanoelectronics, and material science, Physics-Uspekhi **61**, 1175 (2018).

[8] G. Catalan, J. Seidel, R. Ramesh, and J. F. Scott, Domain wall nanoelectronics, Rev. Mod. Phys. **84**, 119 (2012).

[9] A. P. Pyatakov and A. K. Zvezdin, Magnetoelectric and multiferroic media, Phys. Usp. **52**, 557 (2012. Usp. Fiz. Nauk, 182, 593 (2012).

[10] D. Sando, et al., Crafting the magnonic and spintronic response of $BiFeO_3$ films by epitaxial strain, Nat. Mater. **12**, 641 (2013).

[11] A. I. Kurchak, E. A. Eliseev, S. V. Kalinin, M. V. Strikha, and A. N. Morozovska, P-N Junctions Dynamics in Graphene Channel Induced by Ferroelectric Domains Motion, Phys. Rev. Appl. **8**, 024027 (2017).

[12] A. I. Kurchak, A. N. Morozovska, E. A. Eliseev, S. V. Kalinin, and M. V. Strikha, Nontrivial temperature behavior of the carrier concentration in the nanostructure "graphene channel on ferroelectric substrate with domain walls", Acta Mater. **155**, 302 (2018).

[13] W. Wu, L. Wang, Y. Li, F. Zhang, L. Lin, S. Niu, D. Chenet, X. Zhang, Y. Hao, T. F. Heinz, J. Hone, and Z. L. Wang, Piezoelectricity of single-atomic-layer MoS_2 for energy conversion and piezotronics, Nature **514**, 470 (2014).

[14] S. Yuan, X. Luo, H. L. Chan, C. Xiao, Y. Dai, M. Xie, and J. Hao, Room-temperature ferroelectricity in $MoTe_2$ down to the atomic monolayer limit, Nat. Commun. **10**, 1775 (2019).

[15] J. H. Choi and S. H. Jhi, Origin of robust out-of-plane ferroelectricity in d1T-MoS_2 monolayer, J.Phys.: Cond. Matt. **32**, 045702 (2020).

[16] K.-A. N. Duerloo, Y. Li, and E. J. Reed, Structural phase transitions in two-dimensional Mo- and W-dichalcogenide monolayers, Nat. Commun. **5**, 4214 (2014).

[17] A. N. Enyashin, L. Yadgarov, L. Houben, I. Popov, M. Weidenbach, R. Tenne, M. Bar-Sadan, and G. Seifert, New route for stabilization of 1T-WS_2 and MoS_2 phases, J. Phys. Chem. C **115**, 24586 (2011).

[18] G. Eda, T. Fujita, H. Yamaguchi, D. Voiry, D. Chen, and M. Chhowalla, Coherent atomic and electronic heterostructures of single-layer MoS_2, ACS Nano **6**, 7311 (2012).

[19] J. Suh, T. L. Tan, W. Zhao, J. Park, D.-Y. Lin, T.-E. Park, and J. Kim, Reconfiguring crystal and electronic structures of MoS_2 by substitutional doping, Nat. Comm. **9**, 199 (2018).

[20] D. W. Boukhvalov and M. I. Katsnelson, Enhancement of chemical activity in corrugated graphene, J. Phys. Chem. C **113**, 14176 (2009).

[21] S. V. Kalinin and V. Meunier, Electronic flexoelectricity in low-dimensional systems, Phys. Rev. B **77**, 033403 (2008).

[22] P. Johari and V. B. Shenoy, Tuning the electronic properties of semiconducting transition metal dichalcogenides by applying mechanical strains, ACS Nano **6**, 5449 (2012).

[23] J. Berry, S. Zhou, J. Han, D. J. Srolovitz, and M. P. Haataja, Domain morphology and mechanics of the H/T′ transition metal dichalcogenide monolayers, Phys. Rev. Mater. **2**, 114002 (2018).

[24] S. Kang, S. Jeon, S. Kim, D. Seol, H. Yang, J. Lee, and Y. Kim, Tunable out-of-plane piezoelectricity in thin-layered $MoTe_2$ by surface corrugation-mediated flexoelectricity, ACS Appl. Mater. Inter. **10**, 27424 (2018).

[25] J. Berry, S. Zhou, J. Han, D. J. Srolovitz, and M. P. Haataja, Dynamic phase engineering of bendable transition metal dichalcogenide monolayers, Nano Lett. **17**, 2473 (2017).

[26] H. Zhu, Y. Wang, J. Xiao, M. Liu, S. Xiong, Z. J. Wong, Z. Ye, Y. Ye, X. Yin, and X. Zhang, Observation of piezoelectricity in free-standing monolayer MoS_2, Nat. Nanotechnol. **10**, 151 (2015).

[27] M. B. Ghasemian, T. Daeneke, Z. Shahrbabaki, J. Yang, and K. Kalantar-Zadeh, Peculiar piezoelectricity of atomically thin planar structures, Nanoscale **12**, 2875 (2020).

[28] W.-Z. Xiao, H.-J. Luo, and L. Xu, Elasticity, piezoelectricity, and mobility in two-dimensional BiTeI from a first-principles study, J. Phys. D: Appl. Phys. **53**, 245301 (2020).

[29] T. Dumitrica, C. M. Landis, and B. I. Yakobson, Curvature-induced polarization in carbon nanoshells, Chem. Phys. Lett. **360**, 182 (2002).

[30] I. Naumov, A. M. Bratkovsky, and V. Ranjan, Unusual Flexoelectric Effect in Two-Dimensional Noncentrosymmetric sp^2-Bonded Crystals, Phys. Rev. Lett. **102**, 217601 (2009).

[31] W. Shi, Y. Guo, Z. Zhang, and W. Guo, Flexoelectricity in monolayer transition metal dichalcogenides, J. Phys. Chem. Lett. **9**, 6841 (2018).

[32] The adjectives "in-plane" and "out-of-plane" are used here to describe the polarization direction parallel or perpendicular to the surface of a thin film; see, e.g., [N. Setter, D. Damjanovic, L. Eng, G. Fox, Spartak Gevorgian, S. Hong, A. Kingon *et al.* "Ferroelectric thin films: Review of materials, properties, and applications. J. Appl. Phys.100, 051606 (2006)].

[33] M. N. Blonsky, H. L. Zhuang, A. K. Singh, and R. G. Hennig, Ab initio prediction of piezoelectricity in two-dimensional materials, ACS Nano **9**, 9885 (2015).

[34] M. M. Alyörük, Y. Aierken, D. Çakır, F. M. Peeters, and C. Sevik, Promising piezoelectric performance of single layer transition-metal dichalcogenides and dioxides, J. Phys. Chem. C **119**, 23231 (2015).

[35] A. N. Morozovska, E. A. Eliseev, G. I. Dovbeshko, M. D. Glinchuk, Y. Kim, and S. V. Kalinin, Flexo-induced ferroelectricity in low dimensional transition metal dichalcogenides, Phys. Rev. B **102**, 075417 (2020).

[36] A. N. Morozovska, E. A. Eliseev, K. D. Stubbs, R. Vasudevan, Y. Kim, and S. V. Kalinin, Phase diagrams of single layer two-dimensional transition metal dichalcogenides: Landau theory, Phys. Rev. B **101**, 195424 (2020).

[37] G. I. Dovbeshko, Surface enhanced IR absorption of nucleic acids from tumor cells: FTIR reflectance study, Biopolymers (Biospectroscopy) **67**, 470 (2002).

[38] The "effective" force matrix F_{ij}^A is used in the context describing interatomic forces acting between different ions in the harmonic approximation. For a given ion A the matrix consists of the second spatial derivatives of the effective potential $U_A(x_1, x_2, x_3)$ of the ion, $F_{ij}^A = \frac{\partial^2 U_A}{\partial x_i \partial x_j}$. See, e.g., the textbooks [Ch. Kittel, Introduction to solid state physics, London, Chapmen & Hall (1956)], [A.I. Anselm, Introduction to semiconductor theory. Mir, Moscow, Prentice-Hall, Englewood Cliffs, NJ, (1981)].

[39] P. V. Yudin and A. K. Tagantsev, Fundamentals of flexoelectricity in solids, Nanotechnology **24**, 432001 (2013).

[40] K. T. Kang, J. Park, D. Suh, and W. S. Choi, Synergetic behavior in 2D layered material/complex oxide heterostructures, Adv. Mater. **31**, 1803732 (2019).

[41] T. F. Kuech, in *Comprehensive Semiconductor Science and Technology*, edited by P. Bhattacharya, R. Fornari, and H. Kamimura (Elsevier Science, Amsterdam, 2011), Vol. 4. https://www.sciencedirect.com/topics/chemistry/van-der-waals-force

[42] M. Inoue, in *Advanced Adhesives in Electronics*, edited by M. O. Alam and C. Bailey (Woodhead Publishing, Oxford, 2011).

[43] S. P. Koenig, N. G. Boddeti, M. L. Dunn, and J. S. Bunch, Ultrastrong adhesion of graphene membranes, Nat. Nanotechnol. **6**, 543 (2011).

[44] X. Zhaoa, M. Boa, Z. Huangb, J. Zhoua, C. Penga, and L. Li, Heterojunction bond relaxation and electronic reconfiguration of WS_2- and MoS_2-based 2D materials using BOLS and DFT, Appl. Surf. Sci. **462**, 508 (2018).

[45] V. S. Mashkevich and K. B. Tolpygo. Zh.Eksp.Teor.Fiz. **31**, 520 (1957). Sov.Phys. JETP, 4, 455 (1957).].

[46] Sh. M. Kogan, Piezoelectric effect under an inhomogeneous strain and an acoustic scattering of carriers of current in crystals, Solid State Phys. **5**, 2829 (1963).

[47] A. Kvasov and A. K. Tagantsev, Dynamic flexoelectric effect in perovskites from first-principles calculations, Phys. Rev. B **92**, 054104 (2015).

[48] M. D. Glinchuk, A. N. Morozovska, and E. A. Eliseev, Ferroelectric thin films phase diagrams with self-polarized phase and electret state, J. Appl. Phys. **99**, 114102 (2006).

[49] M. D. Glinchuk and A. N. Morozovska, The internal electric field originating from the mismatch effect and its influence on ferroelectric thin film properties, J. Phys.: Condens. Matter **16**, 3517 (2004).

[50] Note that the surface coefficients e^s_{ijk} are usually renormalized by the δz lattice parameter that corresponds to the spacing between 2D layers, i.e., $e^s_{ijk} = \delta z\, e^b_{ijk}$, where e^b_{ijk} are in C/m^2.

[51] A. N. Morozovska, E. A. Eliseev, A. K. Tagantsev, S. L. Bravina, L.-Q. Chen, and S. V. Kalinin, Thermodynamics of electromechanically coupled mixed ionic-electronic conductors: Deformation potential, Vegard strains, and flexoelectric effect, Phys. Rev. B **83**, 195313 (2011).

[52] See Supplemental Material for calculation details, figures and STM results http://link.aps.org/supplemental/10.1103/PhysRevApplied.15.044051.

[53] N. Iguiñiz, R. Frisenda, R. Bratschitsch, and A. Castellanos-Gomez, Revisiting the buckling metrology method to determine the Young's modulus of 2D materials, Adv. Mater. **31**, 1807150 (2019)..

[54] M. Ramos, J. Nogan, M. Ortíz-Díaz, J. L. Enriquez-Carrejo, C. A. Rodriguez-González, J. Mireles-Jr-Garcia, C. Ornelas, and A. Hurtado-Macias, Mechanical properties of RF-sputtering MoS_2 thin films, Surf. Topogr.: Metrol. Prop. **5**, 025003 (2017).

[55] Y. Sun, J. Pan, Z. Zhang, K. Zhang, J. Liang, W. Wang, Z. Yuan, Y. Hao, B. Wang, J. Wang, and Y. Wu, Elastic properties and fracture behaviors of biaxially deformed, polymorphic $MoTe_2$, Nano Lett. **19**, 761 (2019).

[56] L. Yu, Q. Yan, and A. Ruzsinszky, Negative Poisson's ratio in 1T-type crystalline two-dimensional transition metal dichalcogenides, Nat. Commun. **8**, 15224 (2017).

[57] M. Yagmurcukardes, C. Sevik, and F. M. Peeters, Electronic, vibrational, elastic, and piezoelectric properties of monolayer Janus MoSTe phases: A first-principles study, Phys. Rev. B **100**, 045415 (2019).

[58] K.-A. N. Duerloo, M. T. Ong, and E. J. Reed, Intrinsic piezoelectricity in two-dimensional materials, J. Phys. Chem. Lett. **3**, 2871 (2012).

[59] Y. Jin and J. Lee. First-principle Studies of Flexoelectric Effect in Corrugated Two-dimensional Materials. Bulletin of the American Physical Society 65, abstract: M65.00002 (2020).

[60] S. Song, D. H. Keum, S. Cho, D. Perello, Y. Kim, and Y. H. Lee, Room temperature semiconductor–metal transition of $MoTe_2$ thin films engineered by strain, Nano Lett. **16**, 188 (2016).